1    **Fluid escape from subduction zones controlled by channel-forming reactive porosity**

2    Oliver Plümper[1,6], Timm John[2,6], Yuri Y. Podladchikov[3,6], Johannes C. Vrijmoed[4,6], Marco

3                                            Scambelluri[5]

4    [1]Department of Earth Sciences, Utrecht University, Budapestlaan 4, 3584CD Utrecht, The

5    Netherlands

6    [2]Institut für Geologische Wissenschaften, Freie Universität Berlin, Malteserstrasse 74-100,

7    12249 Berlin, Germany

8    [3]Institute of Earth Sciences, University of Lausanne, 1015 Lausanne, Switzerland

9    [4]Department of Earth Sciences, Swiss Federal Institute of Technology Zürich, Sonneggstrasse 5,

10   8092 Zürich, Switzerland

11   [5]Dipartimento di Scienze della Terra, Ambiente e Vita, Università di Genova, Corso Europa 26,

12   16132 Genova, Italy

13   [6]Physics of Geological Processes (PGP), University of Oslo, Blindern, N-0136 Oslo, Norway

14

**ABSTRACT**

Earth would be uninhabitable if water was not returned to exogenous reservoirs at subduction zones, preventing global ocean drainage. Yet the bottleneck mechanism that couples initial fluid release from subducting, zero-porosity rocks with chemically bound water to rocks with high-permeability fluid escape channels is unknown. Using multiscale rock analysis combined with thermodynamic modelling we show that fluid flow initiation in dehydrating serpentinites is controlled by intrinsic chemical heterogeneities, localizing dehydration reactions at specific microsites. Porosity generation is directly linked to the dehydration reactions and resultant fluid-pressure variations force the reactive fluid release to organize into vein networks across a wide range of spatial scales (μm to m). This fluid channelization results in large-scale fluid escape with sufficient fluxes to drain subducting plates. Moreover, our findings suggest that antigorite dehydration reactions do not cause instantaneous rock embrittlement, often presumed as the trigger of intermediate-depth subduction zone seismicity.

30   Within our solar system Earth is the only planet that has both plate tectonics and water. These

31   may not be intuitively linked as the amount of water is extremely small (a few hundred µg/g)

32   compared to the Earth's entire mass. However, water enormously affects Earth's geodynamics

33   and the geochemical cycles of elements at all scales. The most prominent examples of this link

34   between water and plate tectonics are found in subduction zones[1]. In these zones seawater-

35   altered oceanic lithosphere is returned to the mantle, thereby heating up during descent and

36   releasing fluids through the dehydration of hydrous mineral phases. These dehydration reactions

37   (i) facilitate global water fluxes and global mass transfer that trigger mantle melting and fuel

38   explosive volcanism[2,3], (ii) are a source of intermediate-depth seismicity[4,5], and (iii) contribute to

39   slab pull forces through rock densification[6]. As the global water input into subduction zones per

40   million years is on the order of the oceans' total water volume[7,8], efficient, large-scale transport

41   systems need to form in order to drain water from the descendent oceanic plates and return it to

42   exogenous reservoirs. Fluid escape through these transport systems must keep pace with the slab

43   descent velocity of cm/year. Otherwise, even in the presence of other natural outgassing

44   mechanisms (e.g., volcanic hot spots and mid-ocean ridges) the oceans would drain within only a

45   few million years (Methods).

46   If fluid escape was controlled by the low background rock permeability[9,10] at the

47   conditions at which dehydration reactions occur (30 – 300 km, 2 to 10 GPa)[11,12], the resultant

48   slow, static pervasive fluid flow would be insufficient to drain the subducting plates. This

49   conclusion is supported by stable isotope studies that show little evidence for grain-scale fluid

50   migration in exhumed subduction complexes[13,14]. Hence, a dynamic fluid escape mechanism is

51   required that allows fluid flow to organize itself into high-flux transport systems. Although

52   globally documented vein systems in high-pressure metamorphic terrains[15-17] confirm that high

53  fluid fluxes can be achieved through fluid flow channelization, the microscale mechanism that

54  transforms a zero-porosity rock with chemically bound water into a rock characterized by high-

55  permeability channels is yet unknown. Details of this mechanism are important as this is the

56  bottleneck controlling the rate for the entire process of fluid escape from subducting rocks.

57      Here we show how microscale heterogeneities in rock chemistry define the anisotropic

58  evolution of porosity and fluid pressure. Multiscale rock analysis combined with thermodynamic

59  modelling show how this evolution forces water released from dehydrating minerals to

60  instantaneously focus its flow, ultimately leading to high-flux, channelized fluid escape across a

61  wide range of spatial scales (µm to m).

62  **Natural fluid escape networks**

63  In order to develop a theoretical framework to decipher the mechanisms of fluid escape from

64  dehydrating rocks it is necessary to locate natural examples that show the incipient dehydration

65  stages and multiscale evolution of fluid escape routes. As serpentinites are recognized as the

66  main water carriers in subduction zones[18], we selected the Erro-Tobbio meta-serpentinites (ET-

67  MS; Ligurian Alps, Italy) as the leading field example. Unlike any other known locality (e.g.,

68  Cerro de Almirez, Spain[19]), the ET-MS provide a unique snapshot into the incipient dehydration

69  stage[20]. These rocks reveal the multi-scale behavior of the most prominent subduction-zone

70  dehydration reactions, the breakdown of the serpentine phase antigorite ($(Mg,Fe)_3Si_2O_5(OH)_4$; 13

71  wt.% structurally bound water) to anhydrous olivine ($(Mg,Fe)_2SiO_4$). The ET-MS correspond to

72  subcontinental mantle, exhumed and hydrated during the opening of the Jurassic Tethyan ocean,

73  that was involved in Alpine subduction and subsequent high-pressure/low-temperature

74  metamorphism during closure of the oceanic basin[21,22]. The ET-MS display olivine + titanian-

75    clinohumite-bearing vein networks[20-22] formed during partial dehydration of antigorite at peak

76    metamorphic conditions of 2.0-2.5 GPa and 550-650 °C[23] via reactions such as

77                     Antigorite + Brucite = 2 Olivine + 3 $H_2O$      (1)

78    As reaction (1) progress, dehydration results in a significant increase in solid phase density

79    leading to the generation of reaction-induced porosity due to the conservation of solid mass. The

80    preservation of these features at ET-MS makes it an optimal locality to study the onset of rock

81    dehydration, as the rocks did not cross the terminating antigorite-out isograd at ~650 °C (Fig. 1).

82         Prograde olivine-bearing vein networks occur in two settings, (1) as deformed veins

83    within serpentinite mylonites and (2) as veins, minimally affected by deformation, within the

84    bulk serpentinite[21] (Fig. 2). The association of undeformed and deformed veins attests that

85    dehydration-induced vein formation was synchronous with ductile deformation in the enclosing

86    serpentinite mylonites[21]. A striking characteristic of the ET-MS is the strong channelization and

87    coalescence of veins across a wide range of spatial scales (µm-m; Fig. 2). Figure 2a shows a

88    single meter-scale vein being fed by a decimeter-scale vein network (Fig. 2b-d) that originates

89    from millimeter- to micrometer-scale veins (Fig. 2e). To reduce the system's complexity, we

90    herein focus on the undeformed state of the ET-MS vein network in order to extract the essential

91    requirements that drive a dehydrating system into channelization at its earliest stages.

92

## Fluid release within zero-porosity rocks

93   **Fluid release within zero-porosity rocks**

94   The background microstructure of the ET-MS is defined by interlocking blades of antigorite and

95   a very weak foliation. To understand the vein network evolution (Fig. 2) it is necessary to begin

96   with the fluid source regions (FSR) located at the tip of the smallest veins, i.e. the FSRs of first-

97   order dehydration veins without any tributary veins (Fig. 2e; dashed squares). Common to all

98   investigated FSRs (n = 30) is the occurrence of multiple, microporous patches ahead of the vein

99   tip (Fig. 3a), consisting of a polycrystalline aggregate of hydrous phyllosilicate grains

100  (±secondary olivine). Isolated patches range in size from several tens (Fig. 3a) to a few µm (Fig.

101  3b). Individual patches join up via µm-sized seams (Fig. 3b) or overlap to form larger,

102  interconnected areas (Fig. 3c). Both the presence of remnant antigorite within the patches and

103  micro-vein propagation from the patches into the matrix antigorite imply that patches form as a

104  result of reaction-front migration into antigorite during its breakdown. Raman spectroscopy

105  (Supplementary material 2) indicates that the hydrous phyllosilicate described here closely

106  resembles an intermediate phyllosilicate[24] or talc-like[25] phase that has been observed after

107  serpentine dehydration experiments. However, not all serpentinite dehydration experiments[26]

108  have directly identified this phase and thus the exact role of this phase and other prograde

109  phyllosilicate phases (e.g. 10 Å-phase series) in serpentinite dehydration and concurrent porosity

110  generation warrants further investigation. Nevertheless, the formation of this phyllosilicate phase

111  is identified here as an intermediate, prograde reaction step between antigorite breakdown and

112  olivine nucleation due to (i) its occurrence as inclusions within the secondary olivine (Fig. 3d)

113  and (ii) the presence of nanocrystalline, secondary olivine grains within this phase (Fig. 2 e,f).

114  For simplicity we term the phase intermediate - phyllosilicate phase (I-PP).

115    Dislocation substructure analysis of macroscopic olivine grains within the patches reveals

116    extremely low dislocation densities (Supplementary Figure S1). In summary, our observations

117    show that olivine crystals grew at the expense of antigorite, in a textural setting where fluid is

118    transported away from the dehydration front developing cell-like structures (Fig. 3g). Secondary

119    olivine grains are exclusively found within FSRs and veins rather than isolated in the antigorite

120    matrix. In the absence of metamorphic olivine the antigorite matrix is free of porosity. We argue

121    that the key to dehydration initiation in zero-porosity serpentinites is the general production of

122    porosity during reaction (1) or any other serpentinite dehydration reaction that may also co-

123    produce hydrous phyllosilicates (e.g., talc, intermediate talc-like, 10 Å phase) in which a fully

124    anhydrous phase, i.e. (nanocrystalline) olivine, is able to nucleate and grow. This results in a

125    dynamically forming fluid-filled porosity in front of and within the growing and widening vein

126    structures (Fig. 3 d & c). In general, veins show no indicators for repeated hydraulic fracturing

127    (i.e., crack-seal structures) or significant shear displacement, but have microstructures

128    characteristic of reaction-induced porosity generation, compaction and granular flow

129    (Supplementary Figure S2). This observation is in excellent agreement with experimental

130    results[27-30] and indicates that dehydration of initially zero-porosity rocks leads to the rapid

131    development of sufficient permeability via transient, reactive porosity generation rather than

132    exclusively through fracturing.

133    **Fluid production, flow initiation, and channelized fluid escape**

134    To determine the mechanism that controls the bottleneck of channelization after water

135    production within dehydrating, zero-porosity rocks we have conducted a numerical experiment

136    using real, μm-resolved chemical and structural information as our initial input parameters (Fig.

137    4a and Supplementary Material 3). Our primary rock data are taken from a mid-ocean ridge

138  (MOR) serpentinite (ODP Leg 209, Site 1274)[31], the expected precursor rock type for the ET-

139  MS. Microstructures and chemical element distributions (Fig. 4a) of the chosen MOR

140  serpentinite are representative for serpentinized peridotites[32]. Plate tectonic motions carry similar

141  MOR serpentinites to temperature and pressure regimes analogous to those encountered by the

142  ET-MS (Fig. 1; 2.0-2.5 GPa; 550-650 °C). Thus our model picks up where the natural sample,

143  i.e. the MOR serpentinite prior to subduction, left off. However, the model does not take into

144  account chemical modifications through e.g., reactive flow of externally-derived fluids, that may

145  occur during the rock's trajectory from the MOR deep down into the subduction zone.

146      We begin our model with a rock in which all water is stored in antigorite and any

147  preexisting porosity is negligible (zero-porosity case). Increasing temperature initiates

148  dehydration reactions, dividing the rock continuously into a fluid-absent solid and a fluid-filled

149  porosity. Assuming perfect rigidity of the solid grains and, thus, zero solid velocities (the initial

150  undeformed state of the vein network), the conservation of the immobile solid mass (see

151  Methods and Supplementary Material 3.1 for explicit derivations) requires that

152
$$\frac{\partial}{\partial t}\left(\rho_s(1-X_h)\left(1-\varphi_f\right)\right)=0 \qquad (2)$$

153  where $\rho_s$ is solid density (kg m$^{-3}$), $X_h$ is the weight fraction of fluid stored in the solid and $\varphi_f$ is

154  the volume fraction of the fluid-filled porosity. Hence, porosity is simply a function of solid

155  density. Additionally, although the amount of fluid stored in the solid is constrained by

156  thermodynamics, the amount of fluid stored in porosity (i.e. in excess to saturated, mineral-

157  bound fluid) is not and requires the conservation of the total fluid and solid mass. In an open

158  system this results in

159
$$\frac{\partial}{\partial t}\left(\rho_f\varphi_f+\rho_s\left(1-\varphi_f\right)\right)=\nabla\cdot\left(\rho_f\frac{k\varphi_f^{\;3}}{\mu_f}\nabla P_f\right) \qquad (3)$$

160     where $\rho_f$ is fluid density (kg·m$^{-3}$), $k$ permeability (m$^2$), $\mu_f$ fluid viscosity (Pa·s), and $P_f$ fluid

161     pressure (Pa). These two fundamental conservation laws contain five variables of which $\rho_s$, $\rho_f$, $X_h$

162     are thermodynamically constrained and can be calculated as a function of pressure (P),

163     temperature (T), and the effective system composition. Hence, the evolution of the two

164     remaining variables, (i) reaction-induced porosity $\varphi_f$ and (ii) fluid pressure $P_f$, can be determined

165     by two mass balance equations.

166             To capture the microscale evolution of $\varphi_f$ and $P_f$ during the earliest dehydration stage

167     (reaction 1), we compute local thermodynamic equilibria from 300 to 550 °C by Gibbs-free

168     energy minimization, typically used to construct equilibrium phase diagrams[33]. This provides

169     reference tables of $\rho_s$, $\rho_f$, $X_h$ as a function of temperature, pressure and system composition

170     directly based on the µm²-sized compositional heterogeneities of a MOR serpentinite element

171     distribution map (750 µm²). The local system composition used in energy minimization, the

172     effective bulk composition for each µm², is generated by averaging the measured concentrations

173     over the domain size in which mass transport is fast enough to move components to achieve

174     equilibrium. To illustrate the effect of compositional heterogeneity on porosity formation, fluid

175     pressure build up, and flow for a local domain we divided the element distribution map into four

176     different local thermodynamic subdomains (Fig. 4 dashed horizontal and vertical lines;

177     Supplementary Material Fig. S7). Figure 4b shows the equilibrium variation of $X_h$ in P-T space

178     and the two main phase boundaries corresponding to earliest dehydration stage (reaction 1), i.e.

179     olivine-in and brucite-out (examples of the remaining thermodynamic properties can be found in

180     Supplementary Material 3.2). The onset of dehydration (olivine-in) in terms of temperature

181     varies clearly between the subdomains and thus the porosity production coupled to the release of

182     fluid will also vary dependent on the local bulk rock composition. In water-saturated systems $\varphi_f$

9

183    (Fig. 3c) can be obtained from mass balance of the non-volatile solid component (Methods) and

184    $P_f$ (Fig. 3c), for a confined system, from the P-T density maps (Supplementary Material 3.2). In

185    order to track the full microstructural evolution across 750 µm², we define a thermodynamic

186    domain size of 20 µm based on typical serpentine grain size (few nm to several tens of µm),

187    changes in chemical composition, wet grain boundary diffusion-mediated re-equilibration

188    (Methods) and examination of phase assemblages with different averaging scales

189    (Supplementary Material 3.3).

190        The final model (Fig. 5a-c) shows that although reaction progress in a dehydrating rock is

191    an overall function of continuous temperature increase, local variations in the antigorite solid

192    solution composition, specifically the Fe and Al concentration, and the availability of brucite

193    $(Mg[OH]_2)$ and magnetite $(Fe_3O_4)$ force thermodynamically favorable subdomains to react first.

194    This results in a spatiotemporal variability in porosity that is not constrained by thermodynamics,

195    but through mass balance of the immobile solid rock (equation 2). Our model shows that the

196    intrinsic heterogeneities in rock chemistry cause a strong spatiotemporal, microscale variability

197    in $\varphi_f$ and $P_f$, thus permeability where fluid flow occurs, resulting in instantaneous channelization

198    of fluid fluxes during the earliest dehydration stage (Fig. 5a; Supplementary Material 3.4). The

199    heterogeneity of dehydration at the microscale will be further reinforced by interfacial effects,

200    such as a grain-size dependent reactivity[34]. However, this has not been explicitly taken into

201    account in the model presented here. We also do not consider the formation of I-PP in the model

202    as fluid channeling already occurs at the earliest dehydration stage (reaction 1), i.e. the

203    bottleneck stage. Thus, addition of this phase should not change the overall anisotropic porosity

204    and fluid pressure evolution and fluid flow channelization remains defined by microscale

205    heterogeneities in rock chemistry.

206    In conclusion, field observations (Fig. 2) imply that the immediate channelization of

207    reactions and fluid flow, controlled by chemical rock heterogeneities, will guide the overall

208    large-scale fluid escape to remain channelized across at least six orders of magnitude (µm-m).

209    Fluid flow occurs solely in domains with reaction products (Fig. 5b-c) where the vein network is

210    guided by the reaction front geometry rather than by brittle fracturing, in agreement with

211    microstructural observations (Fig. 3). This is highlighted by the similar patterns produced by the

212    purely thermodynamic model (Fig. 5a-b) and the natural dehydration vein network shown in Fig.

213    5d. Any structural heterogeneities existent prior to dehydration, such as foliation[35,36], will aid

214    channelization. Once fluid volumes within evolved fluid escape channels exceed a critical size,

215    rapid and channelized fluid ascent through the subduction zone system will likely be dominated

216    by hydraulic decompaction-compaction phenomena, such as buoyancy-driven porosity

217    waves[37,38], mobile hydrofractures[39] or vug-waves[40].

218

219    **Reactive fluid flow and its influence on channelization**

220    Fluid released during dehydration has a chemical composition in equilibrium with the domain in

221    which it has been liberated. Accordingly, fluid flow has the potential to change the local bulk

222    rock composition along the flow path. To obtain an estimate of the effect of reactive fluid flow

223    on fluid focusing we performed geochemical modeling resulting in a prediction of the fluid

224    species in equilibrium with a serpentinite rock and its influence on the overall dehydration

225    behavior (Supplementary Material 4). Modeling results show that the availability of silica will

226    have a major influence. Increasing the Si:Mg ratio promotes serpentinite dehydration and thus

227    concomitantly increased fluid fluxes. With increasing temperature reactive fluid transport will

228    result in a chemical purification of the olivine vein network, in agreement with natural

229     observations (Fig. 2 & 3). However, intrinsic chemical rock heterogeneities and local fluid

230     pressure variations will dominate the vein network evolution, where reactive transport will

231     amplify the channelization during dehydration.

232     **Consequences for subduction zone fluid escape**

233     The microscale mechanism described here ensures continuous fluid release within a dehydrating

234     plate. This dehydration mechanism is controlled overall by temperature and arises as a

235     consequence of the coupling between chemical heterogeneities, thermodynamics, and fluid-

236     pressure relaxation resulting in an instantaneous fluid flow focus at the onset of dehydration.

237     This indicates that for subduction zone fluid flow processes pervasive porous flow is negligible.

238     Fluid-flow focusing and channelization implies that the global water budget is balanced through

239     large-scale fluid release from the slab that is highly localized in space and time[3,41,42]. These

240     localized flow structures limit the amount of sediment flux melting at the slab-mantle wedge

241     interface, influencing the transfer and recycling of fluid-mobile elements to arc volcano melt

242     source regions. Infiltrating channels crossing this interface will transport highly reactive fluids

243     into the mantle wedge, interacting with the mantle material along the flow path to produce deep,

244     penetrative yet localized mantle metasomatism[43].

245         It has been a long-standing controversy whether or not intermediate-depth seismicity is a

246     direct consequence of dehydration reactions[5,44,45]. Although at first sight the investigated

247     outcrop-scale vein networks may resemble brittle fractures, here we show that dehydration

248     progression via reactive porosity is neither a result of fluid overpressure-induced embrittlement,

249     nor an instantaneous transformation-induced seismic faulting[45]. In contrast, highly localized

250     viscous creep within the identified ultra-fine grained solid reaction products (i.e., nanocrystalline

251     olivine grains; Fig. 3f) could induce a local decrease in effective viscosity leading to thermal

252  runaway shear instabilities[46,57]. Hence, our observations suggest that serpentinite dehydration

253  reactions do not directly lead to seismic failure, in agreement with recent experimental[48,49] and

254  seismological[50] observations.

255

256  **References**

257  1.    Peacock, S. M. Fluid Processes in Subduction Zones. *Science* **248**, 329-337, (1990).

258  2.    Walowski, K. J., Wallace, P. J., Hauri, E. H., Wada, I. & Clynne, M. A. Slab melting

259        beneath the Cascade Arc driven by dehydration of altered oceanic peridotite. *Nat. Geosci.*

260        **8**, 404-408 (2015).

261  3.    John, T. *et al.* Volcanic arcs fed by rapid pulsed fluid flow through subducting slabs. *Nat.*

262        *Geosci.* **5**, 489-492 (2012).

263  4.    Katayama, I., Terada, T., Okazaki, K. & Tanikawa, A. Episodic tremor and slow slip

264        potentially linked to permeability contrasts at the Moho. *Nat. Geosci.* **5**, 731-734 (2012).

265  5.    Hacker, B. R., Peacock, S. M., Abers, G. A. & Holloway, S. D. Subduction factory - 2.

266        Are intermediate-depth earthquakes in subducting slabs linked to metamorphic

267        dehydration reactions? *J. Geophys. Res.-Sol. Ea.* **108**, B1, 2030 (2003).

268  6.    Spence, W. Slab pull and the seismotectonics of subducting lithosphere. *Rev. Geophys.*

269        **25**, 55-69 (1987).

270  7.    van Keken, P. E., Hacker, B. R., Syracuse, E. M. & Abers, G. A. Subduction factory: 4.

271        Depth-dependent flux of $H_2O$ from subducting slabs worldwide. *J. Geophys. Res.-Sol.*

272        *Ea.* **116**, B01401 (2011).

273  8.    Garrison, T. S. *Oceanography, an invitation to marine science*. Vol. 2 (Thomson

274        Brooks/Cole, 2010).

275    9.    Manga, M. *et al.* Changes in Permeability Caused by Transient Stresses: Field
276          Observations, Experiments, and Mechanisms. *Rev. Geophys.* **50**, RG2004 (2012).

277    10.   Ingebritsen, S. E. & Manning, C. E. Permeability of the continental crust: dynamic
278          variations inferred from seismicity and metamorphism. *Geofluids* **10**, 193-205 (2010).

279    11.   Ague, J. J. & Rye, D. M. Simple models of $CO_2$ release from metacarbonates with
280          implications for interpretation of directions and magnitudes of fluid flow in the deep
281          crust. *J. Petrol.* **40**, 1443-1462 (1999).

282    12.   Manning, C. E. & Ingebritsen, S. E. Permeability of the continental crust: Implications of
283          geothermal data and metamorphic systems. *Rev. Geophys.* **37**, 127-150 (1999).

284    13.   Miller, J.A., Cartwright I., Buick, I.S., Barnicoat, A.C. An O-isotope profile through the
285          HP-LT Corsican ophiolite, France and its implications for fluid flow during subduction.
286          Chem. Geol. **178**, 43-69 (2001).

287    14.   Selverstone, J., Sharp, Z.D. Chlorine isotope constraints on fluid-rock interactions during
288          subduction and exhumation of the Zermatt-Saas ophiolite. *Geochem. Geophy. Geosy.* **14**,
289          4370-4391 (2013).

290    15.   Spandler, C., Pettke, T. & Rubatto, D. Internal and External Fluid Sources for Eclogite-
291          facies Veins in the Monviso Meta-ophiolite, Western Alps: Implications for Fluid Flow
292          in Subduction Zones. *J. Petrol.* **52**, 1207-1236 (2011).

293    16.   Breeding, C. M. & Ague, J. J. Slab-derived fluids and quartz-vein formation in an
294          accretionary prism, Otago Schist, New Zealand. *Geology* **30**, 499-502 (2002).

295    17.   Herms, P., John, T., Bakker, R. J. & Schenk, V. Evidence for channelized external fluid
296          flow and element transfer in subducting slabs (Raspas Complex, Ecuador). *Chem. Geol.*
297          **310**, 79-96 (2012).

14

298    18.    Rüpke, L. H., Morgan, J. P., Hort, M. & Connolly, J. A. D. Serpentine and the subduction

299    zone water cycle. *Earth Planet. Sci. Lett.* **223**, 17-34 (2004).

300    19.    Padron-Navarta, J. A. *et al.* Fluid transfer into the wedge controlled by high-pressure

301    hydrofracturing in the cold top-slab mantle. *Earth Planet. Sci. Lett.* **297**, 271-286 (2010).

302    20.    Scambelluri, M., Müntener, O., Hermann, J., Piccardo, G. B. & Trommsdorff, V.

303    Subduction of Water into the Mantle - History of an Alpine Peridotite. *Geology* **23**, 459-

304    462 (1995).

305    21.    Hoogerduijn Strating, E. H. H. & Vissers, R. L. M. Dehydration-Induced Fracturing of

306    Eclogite-Facies Peridotites - Implications for the Mechanical-Behavior of Subducting

307    Oceanic Lithosphere. *Tectonophysics* **200**, 187-198 (1991).

308    22.    Scambelluri, M., Strating, E. H. H., Piccardo, G. B., Vissers, R. L. M. & Rampone, E.

309    Alpine Olivine-Bearing and Titanian Clinohumite-Bearing Assemblages in the Erro

310    Tobbio Peridotite (Voltri-Massif, NW Italy). *J. Metamorph. Geol.* **9**, 79-91 (1991).

311    23.    Messiga, B., Scambelluri, M. & Piccardo, G. B. Chloritoid-Bearing Assemblages in

312    Mafic Systems and Eclogite-Facies Hydration of Alpine Mg-Al Metagabbros (Erro-

313    Tobbio Unit, Ligurian Western Alps). *Eur. J. Mineral.* **7**, 1149-1167 (1995).

314    24.    Chollet, M., Daniel, I., Koga, K. T., Morard, G. & van de Moortele, B. Kinetics and

315    mechanism of antigorite dehydration: Implications for subduction zone seismicity. *J.*

316    *Geophys. Res.-Sol. Ea.* **116**, B04203 (2011).

317    25.    Perrillat, J. P. *et al.* Kinetics of antigorite dehydration: A real-time X-ray diffraction

318    study. *Earth Planet. Sci. Lett.* **236**, 899-913 (2005).

319    26.    Eggler, D.H. & Ehmann A.N. Rate of antigorite dehydration at 2 GPa applied to

320    subduction zones. *Am. Mineral.* 95(5-6):761-769 (2010).

321    27.    Arkwright, J. C., Rutter, E. H., Brodie, K. H. & Llana-Funez, S. Role of porosity and

322           dehydration reaction on the deformation of hot-pressed serpentinite aggregates. *J. Geol.*

323           *Soc. London* **165**, 639-649 (2008).

324    28.    Rutter, E. H., Llana-Funez, S. & Brodie, K. H. Dehydration and deformation of intact

325           cylinders of serpentinite. *J. Struct. Geol.* **31**, 29-43 (2009).

326    29.    Fusseis, F. *et al.* Pore formation during dehydration of a polycrystalline gypsum sample

327           observed and quantified in a time-series synchrotron X-ray micro-tomography

328           experiment. *Solid Earth* **3**, 71-86 (2012).

329    30.    Tenthorey, E. & Cox, S. F. Reaction-enhanced permeability during serpentinite

330           dehydration. *Geology* **31**, 921-924 (2003).

331    31.    Bach, W. *et al.* Unraveling the sequence of serpentinization reactions: petrography,

332           mineral chemistry, and petrophysics of serpentinites from MAR 15° N (ODP Leg 209,

333           Site 1274). *Geophys. Res. Lett.* **33**, L13306 (2006).

334    32.    Plümper, O., Røyne, A., Magrasó, A., Jamtveit, B. The interface-scale mechanism of

335           reaction-induced fracturing during serpentinization. Geology 40, 1103-1106 (2012).

336    33.    Connolly, J. A. D. Computation of phase equilibria by linear programming: A tool for

337           geodynamic modeling and its application to subduction zone decarbonation. *Earth*

338           *Planet. Sci. Lett.* **236**, 524-541 (2005).

339    34.    Emmanuel, S., and Ague, JJ. Impact of nano-size weathering products on the dissolution

340           rates of primary minerals. *Chem. Geol.* **282**, 11-18 (2011).

341    35.    Auzende, A.-L., Escartin, J., Walte, N. P., Guillot, S., Hirth, G., Frost. D.J. Deformation

342           mechanisms of antigorite serpentinite at subduction zone conditions determined from

343     experimentally and naturally deformed rocks. *Earth Planet. Sci. Lett.* **411**, 229-240
344     (2015).

345 36.   Kawano, S., Katayama, I., Okazaki K. Permeability anisotropy of serpentinite and fluid
346     pathways in a subduction zone. *Geology* **39**(10), 939-942 (2011).

347 37.   Connolly, J. A. D. & Podladchikov, Y. Y. Compaction-driven fluid flow in viscoelastic
348     rock. *Geodin. Acta* **11**, 55-84 (1998).

349 38.   Connolly, J. A. D. Devolatilization-generated fluid pressure and deformation-propagated
350     fluid flow during prograde regional metamorphism. *J. Geophys. Res.-Sol. Ea.* **102**,
351     18149-18173 (1997).

352 39.   Bons, P. D. The formation of large quartz veins by rapid ascent of fluids in mobile
353     hydrofractures. *Tectonophysics* **336**, 1-17 (2001).

354 40.   Morgan, J. P. & Holtzman, B. K. Vug waves: A mechanism for coupled rock deformation
355     and fluid migration. *Geochem. Geophy. Geosy.* **6**, 8 (2005).

356 41.   Dragovic, B., Baxter, E. F. & Caddick, M. J. Pulsed dehydration and garnet growth
357     during subduction revealed by zoned garnet geochronology and thermodynamic
358     modeling, Sifnos, Greece. *Earth Planet. Sci. Lett.* **413**, 111-122 (2015).

359 42.   Angiboust, S., Pettke, T., de Hoog, J. C. M., Caron, B. & Oncken, O. Channelized Fluid
360     Flow and Eclogite-facies Metasomatism along the Subduction Shear Zone. *J. Petrol.* **55**,
361     883-916 (2014).

362 43.   Vrijmoed, J. C. *et al.* Metasomatism in the ultrahigh-pressure Svartberget garnet-
363     peridotite (Western Gneiss Region, Norway): Implications for the transport of crust-
364     derived fluids within the mantle. *J. Petrol.* **54**, 1815-1848 (2013).

365   44.   Jung, H. & Green, H. W. Experimental faulting of serpentinite during dehydration: implications for earthquakes, seismic low-velcoity zones, and anomalous hypocenter distributions in subduction zones. *Int. Geol. Rev.* **46**, 1089-1102 (2004).

368   45.   Jung, H., Green, H. W. & Dobrzhinetskaya, L. F. Intermediate-depth earthquake faulting by dehydration embrittlement with negative volume change. *Nature* **428**, 545-549 (2004).

370   46.   John, T. *et al.* Generation of intermediate-depth earthquakes by self-localizing thermal runaway. *Nat. Geosci.* **2**, 137-140 (2009).

372   47.   Kelemen, P. B. & Hirth, G. A periodic shear-heating mechanism for intermediate-depth earthquakes in the mantle. *Nature* **446**, 787-790 (2007).

374   48.   Chernak, L. J. & Hirth, G. Syndeformational antigorite dehydration produces stable fault slip. *Geology* **39**, 847-850 (2011).

376   49.   Proctor, B. & Hirth, G. Role of pore fluid pressure on transient strength changes and fabric development during serpentine dehydration at mantle conditions: Implications for subduction-zone seismicity. *Earth Planet. Sci. Lett.* **421**, 1-12 (2015).

379   50.   Prieto, G. A. *et al.* Seismic evidence for thermal runaway during intermediate-depth earthquake rupture. *Geophys. Res. Lett.* **40**, 6064-6068 (2013).

381

**Author contributions**

All authors participated in collecting the data and interpretation of the results; O.P. and T.J. collected and interpreted the microstructural and chemical data: O.P., T.J., H.V. and Y.Y.P. developed the final model together; T.J. and M.S. did the field work and first petrological sample recognitions.

**Additional information**

Supplementary information is available in the online version of the paper. Reprints and permissions information is available at www.nature.com/reprints. Correspondence and requests for materials should be addressed to O.P. (o.plumper@uu.nl).

**Competing financial interests**

The authors declare no competing financial interests.

**Figure captions**

**Figure 1 Equilibrium phase diagram depicting the metamorphic evolution of a typical serpentinite.** The red box shows the peak metamorphic conditions of the ET-MS, whereas the blue box shows the metamorphic conditions of a typical mid-ocean ridge serpentinite. The earliest dehydration stage (reaction 1) is highlighted by the label 'olivine-in'. To incorporate the effect of $Al_2O_3$ on antigorite stability the most recent antigorite solution model was used (Methods). The bulk rock composition used to calculate the pseudosection can be found in Supplementary material Table S3. Chl: Chlorite; Atg: Antigorite; B: Brucite; Ol: Olivine; Cpx: Clinopyroxene; Opx: Orthopyroxene; Amph: Amphibole; Tlc: Talc; Sp: Spinel; An: Anorthite. Grey scale reflects the degrees of freedom.

**Figure 2 Outcrop and microphotographs of eclogite-facies olivine vein networks as a result of serpentinite dehydration in the Erro-Tobbio area, Italy.** Vein formation during dehydration is a ubiquitous characteristic of the outcrops on all scales, emphasized by the successive zoom-ins into the vein structures from left **a** to right **e**. Inset in **a** and image **c** highlight the channelization of the vein network and arrows mark possible fluid escape routes. **e**, Microphotograph showing first order dehydration veins and representative source regions (dashed square). Scale bars, a-b: 50 cm; d: 5 cm; e: 2 mm.

**Figure 3 Microstructures of fluid source regions ahead of first order dehydration veins. a**, Porous I-PP pockets (red arrows) form in the source region of dehydration veins and are connected by seams that display μm-sized I-PP pockets (red arrows) as in **b**. **c**, Pockets connect to form larger areas where the abundance of secondary olivine increases "downstream". **d**, Olivine-I-PP-antigorite interfacial area, where the secondary olivine incorporates I-PP as

425    inclusions during prograde growth. Porosity and nanocrystalline olivine, shown in **e** and **f,** are

426    concentrated in I-PP areas. Arrows in **f** highlight nanoporosity at I-PP grain contacts**. g**,

427    Magnified view of area highlight in c by white rectangle depicting the development of cell-like

428    drainage structures during prograde dehydration. Scale bars, a: 50 µm; b: 5 µm; c: 50 µm; d: 10

429    µm; e-f: 500 nm; g: 10 µm. Ol: Olivine; Atg: Antigorite; Di: Diopside.

430    **Figure 4 Illustration of the reactive porosity model. a**, Backscattered electron image and Mg

431    element distribution map of a typical mid-ocean ridge serpentinite. The 750 µm² map is divided

432    into four local thermodynamic subdomains for illustrative purposes. **b**, Variation of mineral-

433    bound water $X_h$ as a function of P and T obtained from thermodynamic calculations for each

434    domain in a. **c**, Porosity and fluid pressure calculated from $X_h$, and solid density (equation 11 &

435    12 in Methods) assuming a closed system in the four domains at a ΔT of 100 ℃. White arrows in

436    the fluid pressure map highlight the fluid flow direction and magnitude.

437    **Figure 5 Evolution of the reactive porosity model versus a naturally occurring dehydration**

438    **vein network. a-c**, Numerical model (drained boundary conditions) showing the dehydration of

439    a MOR serpentinite undergoing subduction. 62,500 equilibrium phase diagrams are calculated

440    from X-ray maps (750 µm²) to simulate reaction front, porosity and fluid flux evolution with

441    increasing temperature (Methods). **a**, **b**, Display the distribution and abundance of metamorphic

442    olivine at temperatures of 380 and 530 °C. Intrinsic chemical rock heterogeneities force the

443    reaction front to organize into a vein network with increasing temperature. Fluid flow occurs

444    within the vein network as shown in (**c**). **d**, Pattern matching shows striking similarities between

445    numerical simulations and natural dehydration patterns (ET-MS; 3 mm²). Modeling results are

446    shown on a logarithmic scale.

## Methods

**Ocean drainage calculation.** The total water volume currently stored within all Earth's oceans is $1.4*10^{15}$ metric tons[8]. Calculated global subduction zone water input fluxes, including sediments, igneous crust and mantle, range from $3.6*10^{14}$ to $1*10^{15}$ metric tons/Myr[7,51]. Using a first-order calculation approach, assuming that no water will be able to escape from the subducting slab, all Earth's oceans would be drained within 1.4 to 3.8 Myr.

**Microstructural and spectroscopic investigations.** Back-scattered electron images and electron backscatter diffraction maps were acquired using a JEOL 6610-LV scanning electron microscope. Quantitative element analyses and compositional X-ray mapping was executed in a JEOL JXA8530 Hyperprobe electron microprobe. The accelerating voltage was 15 kV and the beam current 25 nA. A selection of natural and synthetic minerals was used for standardization. Electron-transparent thin foils were prepared for (scanning) transmission electron microscopy ((S)TEM) by using the focused ion beam technique in a FEI FIB200 (GFZ Potsdam, Germany). TEM investigations were carried out in a Zeiss LIBRA 200FE TEM/STEM operating at 200 kV equipped with a high-angle annular dark-field detector. Figure 3 a-d and g show BSE images, e is a high-resolution 'through-the-lens' secondary electron image and f is a high-resolution (HR-)TEM image. Serpentine and associated hydrous phyllosilicate phases were characterized using Raman Spectroscopy. Raman spectra were collected in a Jobin Yvon Xplora Raman microscope using the 532 nm line of a 14 mW Nd-YAG laser. The Raman light was collected in a 180° backscattering geometry and was dispersed by a grating of 1200 grooves/mm after passing through a 50 µm entrance slit. Spectra were acquired in three acquisitions of 100 s in two spectral windows, $100–1175$ cm$^{-1}$ and $3400–3800$ cm$^{-1}$, permitting characterization of the lattice and internal stretching modes as well as the symmetric stretching vibrations of hydroxyls. The

470    spectrometer was calibrated using the first-order Raman band of silica at 520.7 cm$^{-1}$ and the thin

471    section epoxy resin was analysed to check for contributions to the mineral analyses. Raman

472    spectra were deconvoluted by least-squares fitting Gauss-Lorentz functions along with a linear

473    background to the data.

474    **Derivation of reaction-induced, dynamic porosity and fluid pressure evolution.**

475    Conservation of both fluid and solid mass results in

$$\frac{\partial}{\partial t}\left(\rho_f \varphi_f + \rho_s \left(1-\varphi_f\right)\right) + \nabla \cdot \left(\rho_f \varphi_f \overset{r}{V}_f + \rho_s \left(1-\varphi_f\right)\overset{r}{V}_s\right) = 0, \tag{1}$$

477    where $\rho_s$ is solid density, $\rho_f$ fluid density, $\varphi_f$ fluid-filled porosity, $\vec{V}_f$ fluid velocity, $\vec{V}_s$ solid

478    velocity. Conservation of non-hydrous solid is

$$\frac{\partial}{\partial t}\left(\rho_s (1-X_h)\left(1-\varphi_f\right)\right) + \nabla \cdot \left(\rho_s (1-X_h)\left(1-\varphi_f\right)\overset{r}{V}_s\right) = 0, \tag{2}$$

480    where $X_h$ is the weight fraction of fluid stored in the solid rock. Adopting and substituting

481    Darcy's permeability

$$\varphi_f (\overset{r}{V}_f - \overset{r}{V}_s) = -\frac{k\varphi_f^{3}}{\mu_f}\left(\nabla P_f + \rho_f g\right), \tag{3}$$

483    where $k$ is the permeability coefficient in Kozeny-Carman type permeability expression, $\mu_f$ the

484    fluid viscosity, $P_f$ the fluid pressure and $g$ the gravitational acceleration, and assuming zero solid

485    velocity,

$$\vec{V}_s \approx 0 \tag{4}$$

487    into the mass conservation equations (1)-(2) eliminates velocities and results in two equations for

488    two unknowns, namely reaction-induced, fluid-filled porosity $\varphi_f$ and fluid pressure $P_f$

489

$$\begin{cases} \dfrac{\partial}{\partial t}\left(\rho_s(1-X_h)(1-\varphi_f)\right)=0 \\[2mm] \dfrac{\partial}{\partial t}\left(\rho_f\varphi_f+\rho_s(1-\varphi_f)\right)=\nabla\cdot\left(\rho_f\dfrac{k\varphi_f^{\;3}}{\mu_f}\nabla P_f\right) \end{cases}.$$

(5-6)

490    Equilibrium thermodynamics provides the closing relationships for three remaining variables

491

$$\begin{cases} \rho_f=\rho_f(T,P_f,C) \\ \rho_s=\rho_s(T,P_f,C) \\ X_h=X_h(T,P_f,C) \end{cases},$$

(7-9)

492    where $T$ is temperature (K) and $C$ concentration of a specific element (e.g., Fe, Al). The

493    mathematical solution strategy to solve this set of equations can be found in the Supplementary

494    material 3.1.

495    **Initiation of reactive porosity development.** During the initial dehydration stages porosity

496    needs to be created for the generated fluid. As dehydration takes place at depth, fluid pressure

497    rises as a result of the generation of lower density fluid in confined space. The magnitude of this

498    initial fluid pressure rise depends on the potential volume increase of the dehydration reaction. If

499    this varies locally (e.g. due to compositional variability), resulting local over- and under-pressure

500    will initiate spontaneous fluid channelization. Dehydration of the Erro-Tobbio meta-serpentinites

501    starts with antigorite and brucite breakdown to form olivine and fluid. The temperature at which

502    this process initiates is dependent on the bulk rock composition (Table S3). Thermodynamic

503    calculations, using Perple_X[33], are executed under saturated fluid (pure $H_2O$) conditions using

504    the Compensated-Redlich-Kwong (CORK)[52] equation of state for $H_2O$. An antigorite solution

505    model is used to account for the Al-Tschermak's substitution[53]. Other solution models used are

506    Chl(HP), B, Ol(HP), Omph(HP), Opx(HP), Amph(DPW), Sp(HP), Gt(HP), and T for chlorite,

507    brucite, olivine, clinopyroxene, orthopyroxene, amphibole, spinel, garnet and talc, respectively.

508    If due to local compositional variations the antigorite dehydration reaction occurs at different P-

509    T conditions, there will be a spontaneous spatial fluid pressure variation leading to flow. Here,

510    this effect is estimated on the µm-scale.

511    **Thermodynamic calculations on the basis of element distribution maps.** Local bulk

512    compositions are derived from X-ray intensity maps on a µm-scale. The resulting compositional

513    maps (Supplementary Material Fig. S5) are used to model the spontaneous fluid channelization.

514    All elemental maps have been calibrated using quantitative electron microprobe spot analyses

515    (Table S3). A least squares fit of the measured concentrations and pixel intensity of the elemental

516    maps was provided using the backslash operator in Matlab$^{©}$. The pixel intensity used in the

517    calibration was averaged over a 4 µm² area at the location of the spot analyses to account for

518    some analytical error. Results show a good match fit of the predicted compositions of Si, Al, Mg,

519    Fe, Ca on the maps with the spot analyses used for the calibration (Supplementary Material Fig.

520    S6).

521    **Fluid pressure and porosity calculations.** The magnitude of pressure increase for a confined

522    system and a given bulk rock composition can be obtained from P-T density maps. The total

523    density of the system is given by

524
$$\rho_{tot} = \varphi \cdot \rho_f + (1-\varphi) \cdot \rho_s .$$
(10)

525    In water-saturated systems the porosity can be obtained from mass balance of the non-volatile

526    solid components. In the absence of deformation, the porosity is obtained by rearranging the

527    mass balance of non-volatile components:

528
$$\varphi = 1 - \frac{(1-\varphi_0) \cdot \rho_{n0}}{\rho_n} ,$$
(11)

529    where the mass of non-volatile components is given by:

530
$$\rho_n = \rho_s \cdot (1 - X_h).$$
(12)

531   The unknowns in equations (10)-(12) are the fluid and solid density ($\rho_f$, $\rho_s$) and the rock bounded

532   water ($X_h$). These can be obtained with the Perple_X program *werami* from a phase diagram

533   calculated for a given bulk rock composition, spanning the P-T range of interest (see

534   supplementary material Figs S8-10 for results). Two endmember cases for fluid pressure

535   evolution can be considered. In a perfectly confined system density remains constant. For a given

536   temperature change the pressure is determined by following a density contour from a given

537   starting P-T condition. In contrast a perfectly drained system will not lead to pressure build up,

538   but only results in porosity increase. Calculation of the pressure for a confined system at a

539   certain temperature during its dehydration results in a representation of the spatial fluid pressure

540   distribution due to compositional heterogeneity and direction of fluid flow (Fig. 4c).

541   **High-resolution thermodynamic data preparation.** To predict the initiation of porosity,

542   subsequent fluid flow and channelization quantitative modelling, using equations (1)-(9), is

543   applied to the µm-resolved element distribution map. To capture the compositional heterogeneity

544   of the element distribution maps each pixel of the mapped domain can be used as bulk

545   composition and equilibrium phase diagrams can be computed and used to close the system of

546   equations. The local, effective bulk composition for each pixel is dependent on the domain size

547   in which mass transport is fast enough to move components to achieve equilibrium. In order to

548   define an adequate thermodynamic domain size one needs to consider the grain size and changes

549   in chemical composition. Transmission electron microscopy of serpentinite microstructures has

550   shown that serpentine grain sizes are generally between a few nm to several µm[54,55]. Thus,

551   particularly in the presence of fluids[56] mass transport and re-equilibration through grain

552   boundary diffusion will likely affect domains that are on the size of individual serpentinite mesh

553    cores (100-500 µm). To simulate this process, we applied a diffusion algorithm across the

554    element distribution dataset to produce a local effective bulk composition for each pixel.

555    Diffusion is modelled with an explicit 2D finite difference diffusion code with constant diffusion

556    coefficient, D, running with the largest possible stable time step (dt = dx²/D/4). This results in

557    mutual cancelation of all physical parameters like grid spacing, dx, and diffusion coefficient, D,

558    resulting in a four-point averaging stencil as update rule for each time step:

559
$$C_{i,j} = C_{i,j} + dt \cdot D \frac{C_{i+1,j} + C_{i-1,j} + C_{i,j+1} + C_{i,j-1} - 4C_{i,j}}{dx^2} = \frac{C_{i+1,j} + C_{i-1,j} + C_{i,j+1} + C_{i,j-1}}{4} \quad (13)$$

560    In this scheme the number of 'time steps' (number of iterations of the above averaging

561    procedure) define the 'diffusion' length scale as square root of the number of time steps. We find

562    that the optimal diffusion length $L$, without changing the local bulk composition to unrealistic

563    concentrations, is at 20 µm (Supplementary Material 3.3). In order to obtain modelling results

564    within a reasonable timeframe we down-sampled the dataset to 250x250 pixels by averaging

565    over domains of 3x3 µm, resulting in 62,500 phase diagrams. Supplementary material Fig. S11

566    shows a comparison of simulations with different diffusion length scales.

567    **Code availability**

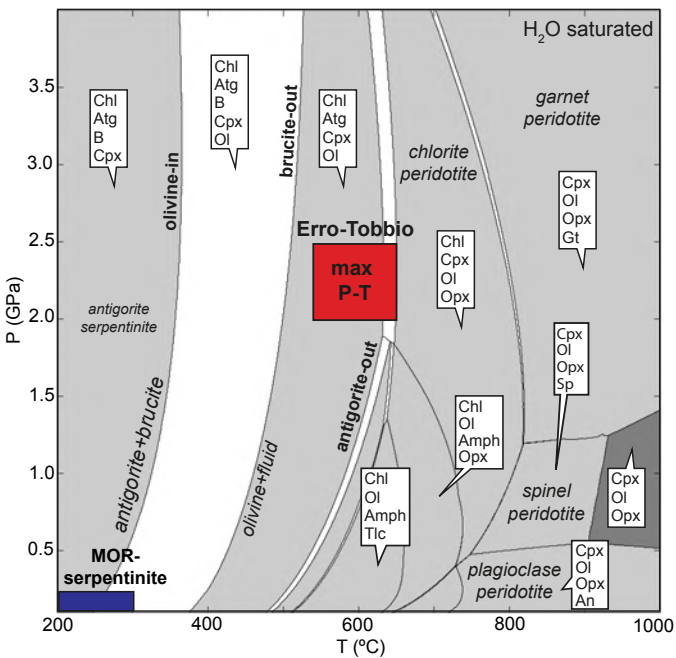568    The code is available upon request to the corresponding author.

569

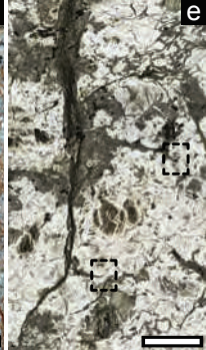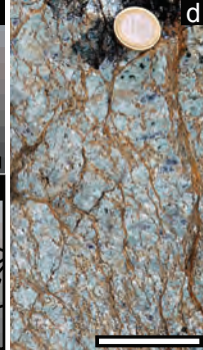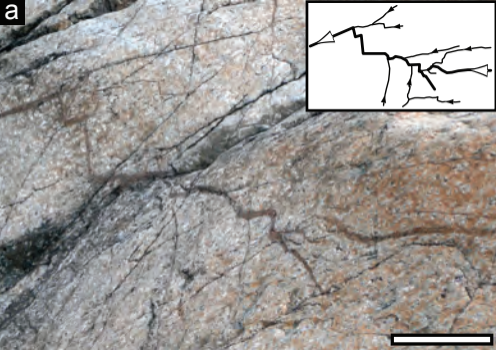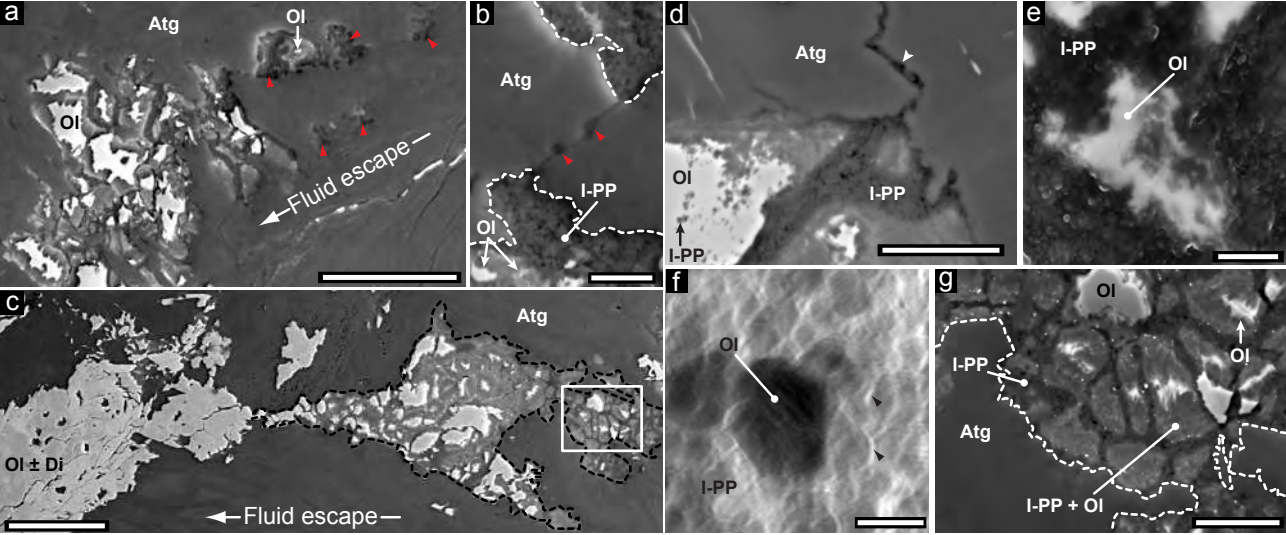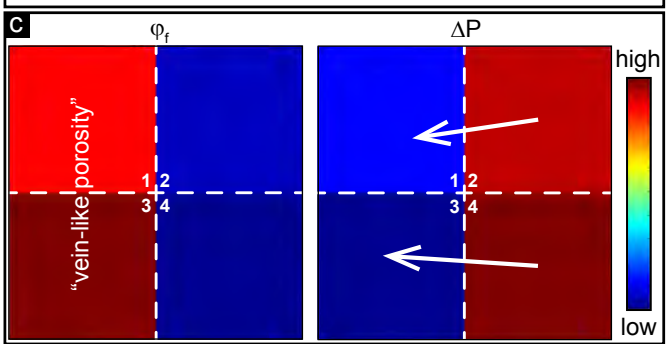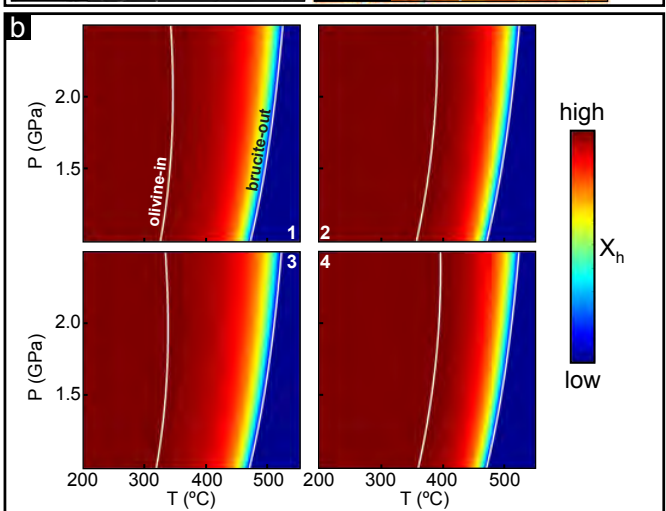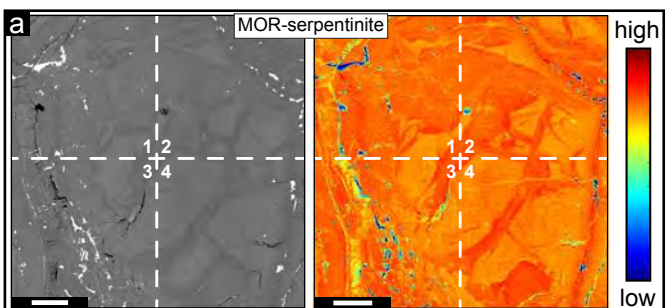570

571

572

**References**

573

574  51.  Parai, R. & Mukhopadhyay, S. How large is the subducted water flux? New constraints

575       on mantle regassing rates. *Earth Planet. Sci. Lett.* **317**, 396-406 (2012).

576  52.  Holland, T. and Powell, R. A Compensated-Redlich-Kwong (CORK) Equation for

577       Volumes and Fugacities of $CO_2$ and $H_2O$ in the Range 1 bar to 50 kbar and 100-1600 °C.

578       *Contrib. Mineral. Petr.* **109**, 265-273 (1991).

579  53.  Padron-Navarta, J.A., Sanchez-Vizcaino, V.L., Hermann, J., Connolly, J.A.D., Garrido,

580       C.J., Gomez-Pugnaire, M.T., Marchesi, C. Tschermak's substitution in antigorite and

581       consequences for phase relations and water liberation in high-grade serpentinites. *Lithos*

582       **178**, 186-196 (2013).

583  54.  Viti, C., Mellini, M. Mesh textures and bastites in the Elba retrograde serpentinites. *Eur.*

584       *J. Mineral.* **10**, 1341-1359 (1998).

585  55.  Dodony, I., Buseck, P. R. Serpentines close-up and intimate: An HRTEM view. *Int. Geol.*

586       *Rev.* **46**, 507-527 (2004).

587  56.  Dohmen, R., Milke, R.. Diffusion in polycrystalline materials: grain boundaries,

588       mathematical models, and experimental data, in: Zhang, Y., Cherniak, D.J. (Eds.),

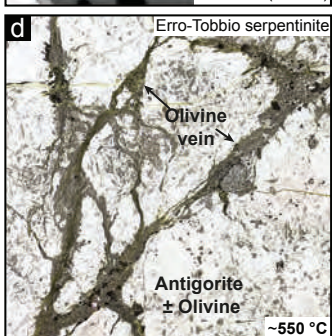589       *Reviews in Mineralogy & Geochemistry*, pp. 921-970 (2010).
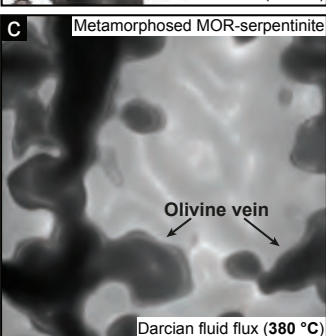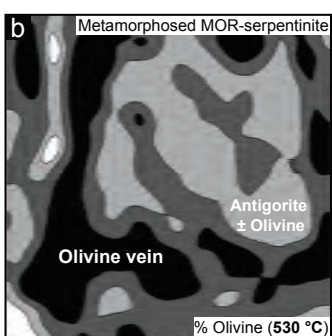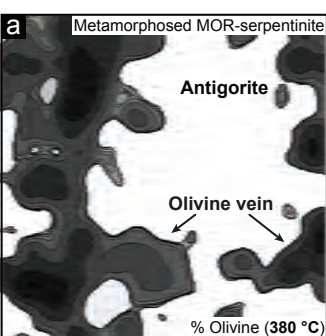
590

**a**  MOR-serpentinite

1 2
3 4

high

low

**b**

P (GPa)

olivine-in    brucite-out

1

2

high

$X_h$

low

P (GPa)

3

4

200   300   400   500
T (°C)

200   300   400   500
T (°C)

**c**

$\varphi_f$    $\Delta P$

"vein-like porosity"

1 2
3 4

1 2
3 4

high

low

**a** Metamorphosed MOR-serpentinite

**Antigorite**

**Olivine vein**

% Olivine (**380 °C**)

**b** Metamorphosed MOR-serpentinite

**Antigorite ± Olivine**

**Olivine vein**

% Olivine (**530 °C**)

**c** Metamorphosed MOR-serpentinite

**Olivine vein**

Darcian fluid flux (**380 °C**)

**d** Erro-Tobbio serpentinite

**Olivine vein**

**Antigorite ± Olivine**

~**550 °C**

low        high